The Astrophysical Journal, 998:216 (16pp), 2026 February 20 https://doi.org/10.3847/1538-4357/ae3757

A Comprehensive Photometric Study of the Eclipsing SU UMa-type Cataclysmic Variable OY Carinae

Zhong-Tao Han[1], Sheng-Bang Qian[2], Fernández Lajús Eduardo[3,4], Wei-Wei Na[1], Hu-Shang Xu[1], Soonthornthum Boonrucksar[5], Ai-Jun Dong[6], and Ting-Ting Yang[1]
[1] Faculty of Mathematics and Physics, Yuxi Normal University, Phoenix Road 134, 653100 Yuxi, People's Republic of China; hzt@yxnu.edu.cn
[2] Department of Astronomy, School of Physics and Astronomy, Key Laboratory of Astroparticle Physics of Yunnan Province, Yunnan University, Kunming 650091, People's Republic of China
[3] Facultad de Ciencias Astronómicas y Geofísicas, Universidad Nacional de La Plata, Paseo del Bosque s/n, 1900 La Plata, Buenos Aires, Argentina
[4] Instituto de Astrofísica de La Plata (CCT La Plata CONICET/UNLP), 1900 La Plata, Argentina
[5] National Astronomical Research Institute of Thailand, Ministry of Higher Education, Science Research and Innovation, 260 Moo 4, T. Donkaew, A. Maerim, Chiangmai, 50180, Thailand
[6] Guizhou Provincial Key Laboratory of Radio Data Processing, School of Physics and Electronic Sciences, Guizhou Normal University, Guiyang 550001, People's Republic of China
Received 2025 August 7; revised 2025 December 25; accepted 2026 January 10; published 2026 February 11

Abstract

We present a comprehensive photometric study of the eclipsing dwarf nova OY Car based on ground-based observations and archival data from the Transiting Exoplanet Survey Satellite (TESS) and AAVSO. Eclipse timing analysis reveals a secular increase in the orbital period at a rate of $+5.70 \times 10^{-13}$ s s^{-1}, superimposed with a cyclic variation with an amplitude of 57.11 s and a period of 33.41 yr. This period increase cannot be attributed to either mass transfer or a period bouncer, suggesting the presence of an unrecognized mechanism. The cyclic oscillation is most effectively interpreted as a gravitational perturbation from an undetected circumbinary object. The potential tertiary companion is estimated to be a giant planet with a mass of $11.5(\pm3.1)M_{\rm Jup}$ in a circular orbit. The TESS light curve captures one superoutburst and one normal outburst. Analysis of the eclipse depth versus the out-of-eclipse flux reveals a linear correlation during quiescence, but with a lower slope before the superoutburst, consistent with disk structure changes predicted by the thermal-tidal instability model. Deviations from linearity during outbursts manifest as hysteresis loops, indicative of significant disk expansion. Eclipse analysis reveals that the normal outburst is of the outside-in type, while the superoutburst exhibits a quasi-periodic $O-C$ modulation indicating a precessing eccentric disk. We derive a mean superhump period of 0.06456 day via the beat relation, which yields a mass ratio of $q = 0.1049$ using an empirical relation. We also study the superhump evolution, identifying the standard three-stage evolution. The positive period derivative in stage B and the discrepancy between dynamical and empirical mass ratio estimates confirm the significant influence of pressure effects on the accretion disk precession.

Unified Astronomy Thesaurus concepts: Close binary stars (254); Compact binary stars (283); Interacting binary stars (801); Eclipsing binary stars (444); Cataclysmic variable stars (203); Dwarf novae (418); SU Ursae Majoris stars (1645)

1. Introduction

Accreting white dwarfs are commonly observed within close binary systems, featuring orbital periods spanning from a few minutes to several hours. The white dwarf star accretes material from a companion star, which can be either a main-sequence star or another white dwarf. Through the accretion process, the material from the companion star forms an accretion disk around the white dwarf, leading to a variety of astrophysical phenomena such as novae, dwarf novae, and AM CVn stars. As a type of accreting white dwarf binaries, the dwarf novae often show optical outbursts with amplitudes of 2–8 mag, with recurrence times ranging from days to decades (see B. Warner 2003). The outburst mechanism is likely the release of gravitational energy due to a thermal-viscous instability in the accretion disk, associated with the partial ionization of hydrogen (see Y. Osaki 1996; J.-P. Lasota 2001). Additionally, some dwarf novae exhibit outbursts with durations spanning approximately two weeks to a month, which are slightly brighter than normal outbursts and are referred to as superoutbursts. Such phenomena are attributed to a combination of the thermal instability and tidal interaction of the disk with the donor star (Y. Osaki 1989). More specifically, the former triggered a normal dwarf nova outburst, resulting in the expansion of the disk radius up to a critical value (i.e., 3:1 resonance radius) where the disk became tidally unstable and a superoutburst occurred. The most prominent feature of superoutbursts is the presence of superhumps, which are periodic brightness modulations with periods several percent longer or shorter than the orbital period of the system, corresponding to positive and negative superhumps, respectively (e.g., N. Vogt 1974, 1982; C. Motch 1981; M. A. Wood et al. 2011). The origin of positive superhumps is the precession of an elliptical and asymmetric disk produced by the tidal torques from the secondary star (R. Whitehurst 1988; R. Whitehurst & A. King 1991), and the negative superhumps are believed to result from the precession of the tilted accretion disk (e.g., J. M. Bonnet-Bidaud et al. 1985; D. Harvey et al. 1995; J. Patterson 1999; M. M. Montgomery 2009; M. A. Wood et al. 2009; M. Kimura & Y. Osaki 2021).

The superoutburst is one of the most important hallmarks in identifying the SU UMa-type dwarf novae. OY Carinae (hereafter OY Car) is an eclipsing SU UMa-type star with a short binary period of 1.51 hr and has been extensively studied in the last few decades at wavelengths ranging from the optical to X-rays (e.g., I. Billington et al. 1996; C. W. Mauche 1998; C. W. Mauche & J. C. Raymond 2000; G. Ramsay et al. 2001a, 2001b; D. S. Baskill et al. 2005; D. Pandel et al. 2005; P. A. Woudt & B. Warner 2009; C. M. Copperwheat et al. 2012). Its superoutbursts have been observed photometrically by W. Krzeminski & N. Vogt (1985), R. Schoembs (1986), A. Bruch et al. (1996), and G. W. Pratt et al. (1999). The properties of the superhumps in OY Car have also been studied in the following years (e.g., J. Smak 2013; T. Kato et al. 2017 and references therein). However, early ground-based observations suffer from a few drawbacks in probing the outburst properties and light curve morphology, as well as in investigating the superhump evolution due to the randomized gaps and the limited length of nightly light curves. The continuous monitoring by the Transiting Exoplanet Survey Satellite (TESS; G. R. Ricker et al. 2014) has allowed these problems to be overcome, enabling a test of the theory of dwarf nova outbursts.

Another distinct feature in the light curves of OY Car is the deep eclipses due to the high orbital inclination (~83°; J. H. Wood et al. 1989; M. McAllister et al. 2019). This property can constrain the binary parameters well and reveal orbital period variations, which provide an opportunity to test the evolutionary theory of cataclysmic variables (CVs) and to pick up circumbinary companions. Moreover, the eclipse proves to be a valuable tool for the investigation of accretion disks. For example, K. Horne (1985) proposed the eclipse mapping method to address the problem of the disk evolution with time during outburst (see R. Baptista 2016 for a detailed overview). As a result, based on the above characteristics, OY Car is an interesting object that can be used to explore the nature of accreting white dwarfs in CVs.

In this paper, we report the ground-based and TESS photometry of OY Car, and then we present a detailed analysis of the optical variability of this system, including eclipse timings, normal outbursts, and superoutbursts. We describe the observations in Section 2. We perform a study of the orbital period variations and an analysis of TESS photometry of OY Car in Section 3. We discuss the physical causes of the eclipse timing variations and the outburst properties in Section 4. The results are summarized in Section 5.

2. Data

2.1. Ground-based Photometry

OY Car was monitored photometrically from 2008 November to 2025 February with the 2.15 m Jorge Sahade telescope at the Complejo Astronomico El Leoncito (CASLEO), San Juan, Argentina. This telescope is equipped with a VersArray 2048B CCD camera manufactured by Roper Scientific, Princeton Instruments. The field view of the telescope is $5\overset{'}{.}1 \times 5\overset{'}{.}1$. No filter was used during the observations in order to improve the time resolution. The star was observed for ~20–120 minutes each night with a 4–5 s exposure time bring about a cadence of ~9 s. The standard reduction of the data was performed using the aperture photometry package of the IRAF software (see D. Tody 1986, 1993). Processing consists of the basic processing steps by subtracting bias, dark, and correcting the flat-field. We used the differential photometry method to extract the light curves. The comparison star is the same for all observations and has been checked to be a nonvariable star. Eight eclipse profiles during quiescence are shown in Figure 1. This eclipse shape exhibits a two-step characteristic, which implies that the ingress and egress times of the white dwarf can be distinguished clearly. The detectability of the white dwarf's ingress and egress features enables us to accurately measure the time of inferior conjunction, which can differ significantly from the time of minimum light. To ensure the precision and homogeneity of the eclipse timings, we consistently applied the derivative method proposed by J. H. Wood et al. (1985) to all light curves presented in this work. This technique determines the mid-eclipse time by locating the times of mid-ingress and mid-egress of the white dwarf, corresponding to the extrema of the light curve's derivative. Unlike polynomial fitting to the eclipse bottom, which can be skewed by the variable contribution of the bright spot or accretion disk asymmetries, the derivative method relies on the sharp, stable geometric features of the white dwarf's occultation. This method has been successfully applied to various eclipsing CVs to reveal precise orbital changes (e.g., S. B. Qian et al. 2015; Z.-T. Han et al. 2017, 2023). Furthermore, to address the systematic discrepancies raised in previous studies (e.g., L. Pilarčík et al. 2018; B. E. Schaefer 2024), we have reexamined and recalculated the eclipse times from our previous dataset (Z.-T. Han et al. 2015) using this consistent derivative method. The results are listed in Table 1.

2.2. American Association of Variable Star Observers Data

We inspected the light curves of OY Car retrieved from the American Association of Variable Star Observers (AAVSO) International Database[7] and obtained a long photometric time series data. Figure 2 plots the long-term AAVSO light curves in the Vis/V band, spanning a total of 60.4 yr between 1963 June 26 and 2023 November 13. Note that the unreliable observations in the Vis have been excluded. The light curves are characterized by two main types of variability: outbursts and eclipses, and the former can also be divided into superoutbursts and normal outbursts. The quiescent magnitude is very difficult to accurately measure due to the variations in the out-of-eclipse brightness and the eclipses. We roughly estimate a quiescent level of ~15.4 mag. In addition, the light curve in the V band during quiescence contains many eclipses, which can be used for eclipse timings. The bottom panel of Figure 2 shows an enlarged view of the segment enclosed by the red rectangle. Using the same method above, 17 mid-eclipse times are obtained and also listed in Table 1. Likewise, these mid-eclipse times are also converted to Barycentric Julian Dates in Barycentric Dynamical Time (BJD_TDB).

2.3. TESS Observations

The main goal of the TESS is to detect small transiting planets that orbit bright stars (G. R. Ricker et al. 2015, 2016; K. A. Collins et al. 2018). TESS observes in sectors, in which each sector, totaling 27.4 days, is separated into two continuous observation orbits of ~13.7 days and interrupted

[7] https://www.aavso.org/LCGv2/

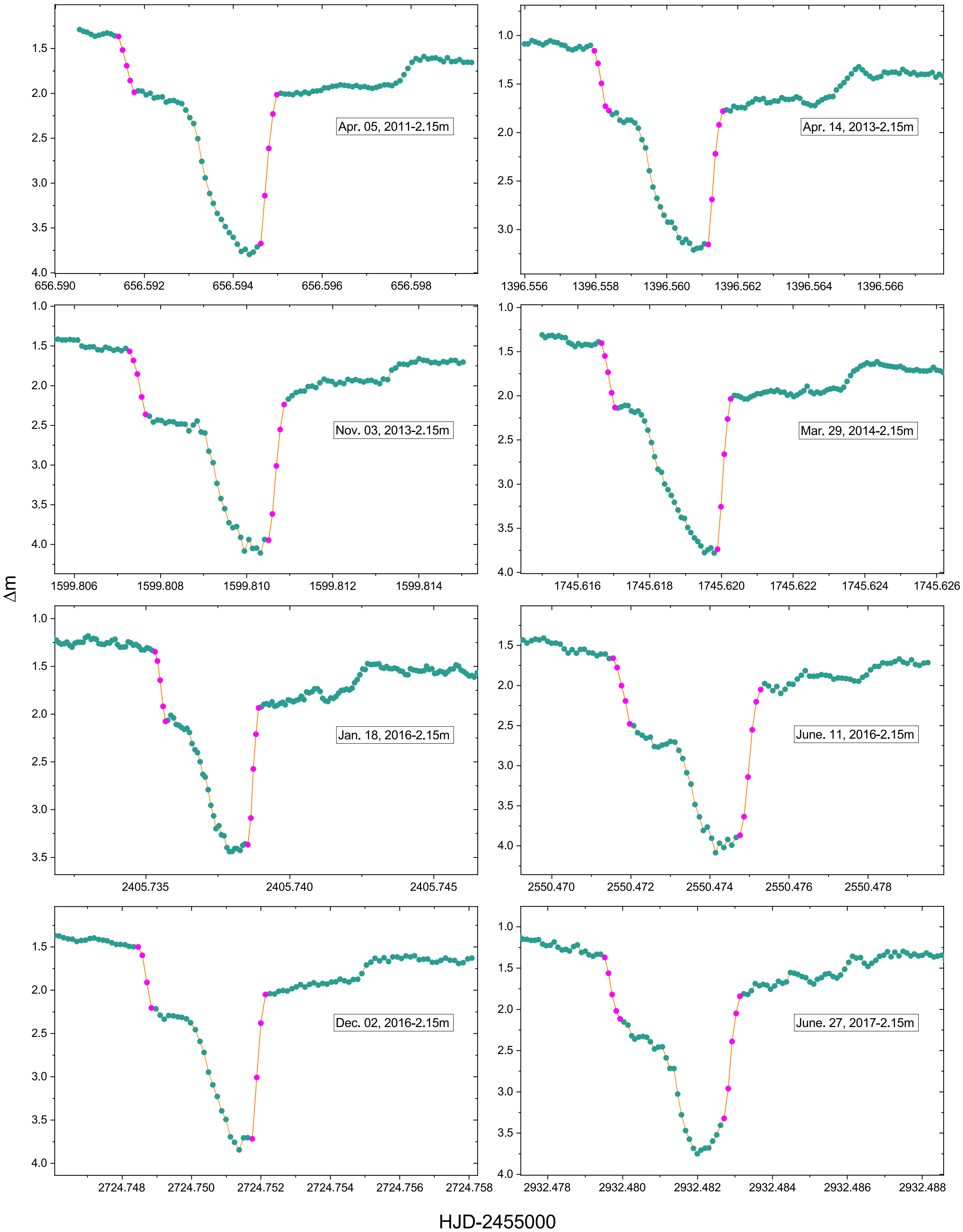

Figure 1. Eight sample eclipse light curves of OY Car during quiescence in the *N* band observed with the 2.15 m Jorge Sahade telescope in Argentina. The eclipse light curves display the properties of the white dwarf and bright spot eclipses. The magenta refers to the ingress and egress of the white dwarf.

briefly to download the data. Generally, the duration of dwarf nova outbursts is ∼2–20 days. Therefore, TESS data allow us to explore the properties of outbursts and oscillations with time in CVs (e.g., J. M. C. Court et al. 2019; Z.-T. Han et al. 2021). TESS observed OY Car during Cycle 1 (2019 March 26–2019 May 20), during Cycle 3 (2019 April 2–2021 May 26), and during Cycle 5 (2023 April 6–2023 June 1) at a 2 minute cadence. The light curves were downloaded from the Mikulski Archive for Space Telescopes web service.[8] Note that we have considered only the data with the quality flag value of 0 in this work. Figure 3 displays the observed TESS Cycle 1 and 3 (Sectors 11 and 37) light curves of OY Car, showing a superoutburst lasting ∼18 days and a normal outburst lasting ∼4 days. The detrended light curve by subtracting the outburst

[8] https://mast.stsci.edu/portal/Mashup/Clients/Mast/Portal.html

Table 1
New Mid-eclipse Times of OY Car

Date	Min. (HJD)	Min. (BJD)	Epoch	$O-C$ (days)	Err (days)	Telescopes	Filters
2008 Nov 28	2454798.84312	2454798.84387	171184	−0.00218	0.00005	2.15 m	*N*
2009 Jan 14	2454845.67889	2454845.67965	171926	−0.00213	0.00005	2.15 m	*N*
2010 Apr 8	2455295.09965	2455295.10042	179046	−0.00233	0.00010	AAVSO	*V*
2010 Apr 8	2455295.16285	2455295.16362	179047	−0.00226	0.00010	AAVSO	*V*
2010 Apr 8	2455295.22595	2455295.22672	179048	−0.00228	0.00010	AAVSO	*V*
2010 Dec 6	2455536.85361	2455536.85438	182876	−0.00152	0.00020	2.15 m	*N*
2010 Dec 7	2455537.80018	2455537.80096	182891	−0.00175	0.00020	2.15 m	*N*
2011 Apr 3	2455654.57336	2455654.57413	184741	−0.00229	0.00005	2.15 m	*N*
2011 Apr 5	2455656.59318	2455656.59395	184773	−0.00233	0.00005	2.15 m	*N*
2012 Apr 15	2456033.48817	2456033.48894	190744	−0.00238	0.00005	2.15 m	*N*
2013 Apr 13	2456395.67604	2456395.67682	196482	−0.00237	0.00005	2.15 m	*N*
2013 Apr 14	2456396.55972	2456396.56050	196496	−0.00238	0.00005	2.15 m	*N*
2013 Nov 3	2456599.80910	2456599.80988	199716	−0.00237	0.00005	2.15 m	*N*
2013 Nov 5	2456601.82896	2456601.82974	199748	−0.00238	0.00005	2.15 m	*N*
2014 Mar 29	2456745.61846	2456745.61924	202026	−0.00235	0.00005	2.15 m	*N*
2014 Mar 30	2456746.69148	2456746.69226	202043	−0.00238	0.00005	2.15 m	*N*
2014 Mar 31	2456747.63831	2456747.63909	202058	−0.00237	0.00005	2.15 m	*N*
2015 Jan 3	2457026.19087	2457026.19165	206471	−0.00244	0.00010	AAVSO	*V*
2016 Jan 16	2457403.84351	2457403.84429	212454	−0.00229	0.00005	2.15 m	*N*
2016 Jan 18	2457405.73711	2457405.73789	212484	−0.00232	0.00005	2.15 m	*N*
2016 Jan 19	2457406.62083	2457406.62161	212498	−0.00229	0.00005	2.15 m	*N*
2016 Jun 10	2457549.52665	2457549.52743	214762	−0.00225	0.00005	2.15 m	*N*
2016 Jun 11	2457550.47339	2457550.47417	214777	−0.00232	0.00005	2.15 m	*N*
2016 Jun 12	2457551.54648	2457551.54726	214794	−0.00229	0.00005	2.15 m	*N*
2016 Oct 11	2457672.86490	2457672.86568	216716	−0.00227	0.00005	2.15 m	*N*
2016 Dec 2	2457724.75033	2457724.75110	217538	−0.00225	0.00005	2.15 m	*N*
2017 Jun 27	2457932.48127	2457932.48206	220829	−0.00226	0.00005	2.15 m	*N*
2017 Nov 16	2458074.18781	2458074.18860	223074	−0.00219	0.00010	AAVSO	*V*
2017 Nov 16	2458074.25093	2458074.25172	223075	−0.00219	0.00010	AAVSO	*V*
2017 Nov 24	2458082.14109	2458082.14189	223200	−0.00214	0.00010	AAVSO	*V*
2017 Nov 24	2458082.20416	2458082.20495	223201	−0.00219	0.00010	AAVSO	*V*
2017 Nov 25	2458083.15104	2458083.15183	223216	−0.00213	0.00010	AAVSO	*V*
2017 Nov 25	2458083.21399	2458083.21479	223217	−0.00230	0.00010	AAVSO	*V*
2018 Jan 18	2458137.11940	2458137.12019	224071	−0.00216	0.00010	AAVSO	*V*
2018 Jan 18	2458137.18251	2458137.18330	224072	−0.00217	0.00010	AAVSO	*V*
2018 Jan 18	2458137.24566	2458137.24645	224073	−0.00214	0.00010	AAVSO	*V*
2018 Jan 19	2458138.12935	2458138.13014	224087	−0.00214	0.00010	AAVSO	*V*
2018 Jan 19	2458138.19248	2458138.19327	224088	−0.00213	0.00010	AAVSO	*V*
2018 Jan 19	2458138.25558	2458138.25637	224089	−0.00216	0.00010	AAVSO	*V*
2019 Jun 6	2458640.50884	2458640.50964	232046	−0.00209	0.00005	2.15 m	*N*
2023 Jan 25	2459970.21465	2459970.21547	253112	−0.00164	0.00010	AAVSO	*V*
2023 May 25	2460089.51337	2460089.51419	255002	−0.00146	0.00005	2.15 m	*N*
2025 Feb 23	2460729.81213	2460729.81294	265146	−0.00136	0.00005	2.15 m	*N*

shape is also plotted in Figure 3. We can clearly see that the eclipse depth undergoes a significant change over the outburst cycle, and the superhumps appeared at the superoutburst peak. The nature of outbursts and eclipses will be studied and discussed in the following sections.

3. Data Analysis and Results

3.1. Improved Orbital Ephemeris

Several studies have been published that investigate the orbital period changes of OY Car (e.g., N. Vogt et al. 1981; M. C. Cook 1985; J. H. Wood et al. 1989; J. G. Greenhill et al. 2006; Z.-T. Han et al. 2015; L. Pilarčík et al. 2018; B. E. Schaefer 2024). In several studies before 2006, the orbital period of OY Car showed no obvious changes. In 2006, J. G. Greenhill et al. found that the orbital period of OY Car has a possible sinusoidal variation of ∼35 yr in the $O-C$ diagram. Z.-T. Han et al. (2015) performed a period change study of OY Car and confirmed that its orbital period may indeed have a periodic oscillation, but the period is only 14 yr. L. Pilarčík et al. (2018) further updated the $O-C$ curve and improved the sinusoidal ephemeris with the period of the modulation 29 or 28 yr. Recent work from B. E. Schaefer (2024) reevaluated the eclipse timing data and concluded that the variations are inconsistent with a simple, stable planetary model. Regarding the eclipse times from the TESS data reported by B. E. Schaefer (2024), we note that the exposure time of 120 s is significantly longer than the typical duration of the white dwarf's ingress/egress (∼40–60 s). Such low time resolution smears out the sharp contact features required for precise $O-C$ analysis. While folding data over an entire sector can improve the signal-to-noise ratio, it averages out the intrinsic eclipse-to-eclipse timing jitter and potential short-term variations. Therefore, to maintain the high temporal precision and consistency of our $O-C$ analysis,

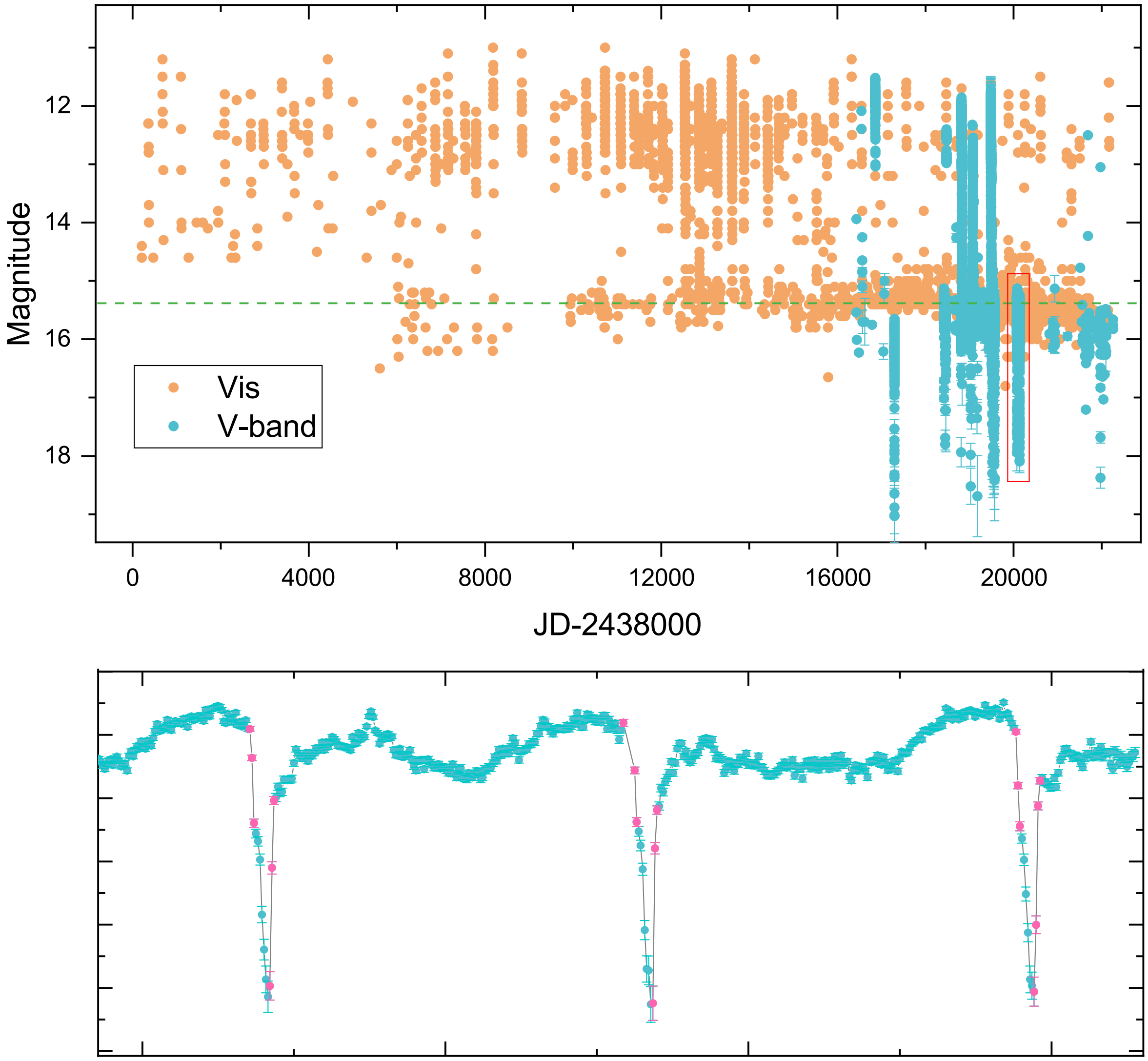

Figure 2. Archival AAVSO light curve of OY Car during 1963 June 26 to 2023 November 13. The cyan solid circles represent the *V*-band data, and the orange solid circles correspond to the visual observations. The light curve in the lower panel is a zoom to a part of the *V*-band data, displaying clear white dwarf eclipses.

we have excluded the low-resolution TESS eclipse timings derived from folded light curves. The latest $O-C$ diagram was constructed by using the ephemeris from J. H. Wood et al. (1989)

$$\text{Min.(BJD)} = 2443993.553813(9) + 0.0631209239(5) \times E. \quad (1)$$

Figure 4 shows the updated $O-C$ curve, which has an approximately 46 yr observational baseline. We have tried several solutions to fit these data, including the linear and/or quadratic plus sinusoidal model, and the linear and/or quadratic plus light travel time effect (LTTE) model. The results show that a quadratic plus sinusoidal ephemeris is the best solution, which can be represented by the following equation:

$$O - C = \Delta T_0 + \Delta P_0 \times E + \beta E^2 + K \sin(2\pi/P_3 + \varphi), \quad (2)$$

where $\beta = 0.5\dot{P}P$ represents the coefficient of the quadratic term, and $\dot{P}$ is the rate of period change. Table 2 provides a summary of the fitting parameters and errors acquired by using the Levenberg–Marquardt method (W. H. Press et al. 1992). The weights are the inverse of the squared data point error. The fitted curve is also plotted in Figure 4. A small residual sum of squares (RSS $= 9.77 \times 10^{-7}$) indicates that this is a good fit, although there are some deviations in the range of 50,000–150,000 cycles. We will discuss the possible reasons for the departure in Section 4.1. The result shows that the orbital period of OY Car, in addition to the long-term increase, also has a cyclic oscillation with an amplitude of 57.11($\pm$0.86) s and a period of 33.41 ($\pm$0.06) yr, which significantly revises the previous planetary parameters. A separate subsection, Section 4.1.3, has been added to provide a thorough comparison and discussion of our results in the context of prior studies. In Figure 4, the best-fitting ephemeris is indicated by the orange solid line in the top panel. The residuals from such a best-fitting model are plotted in the bottom panel.

3.2. TESS Photometry Analysis

TESS light curves of OY Car are extremely diverse and complex, including outbursts, superhumps, oscillations, and

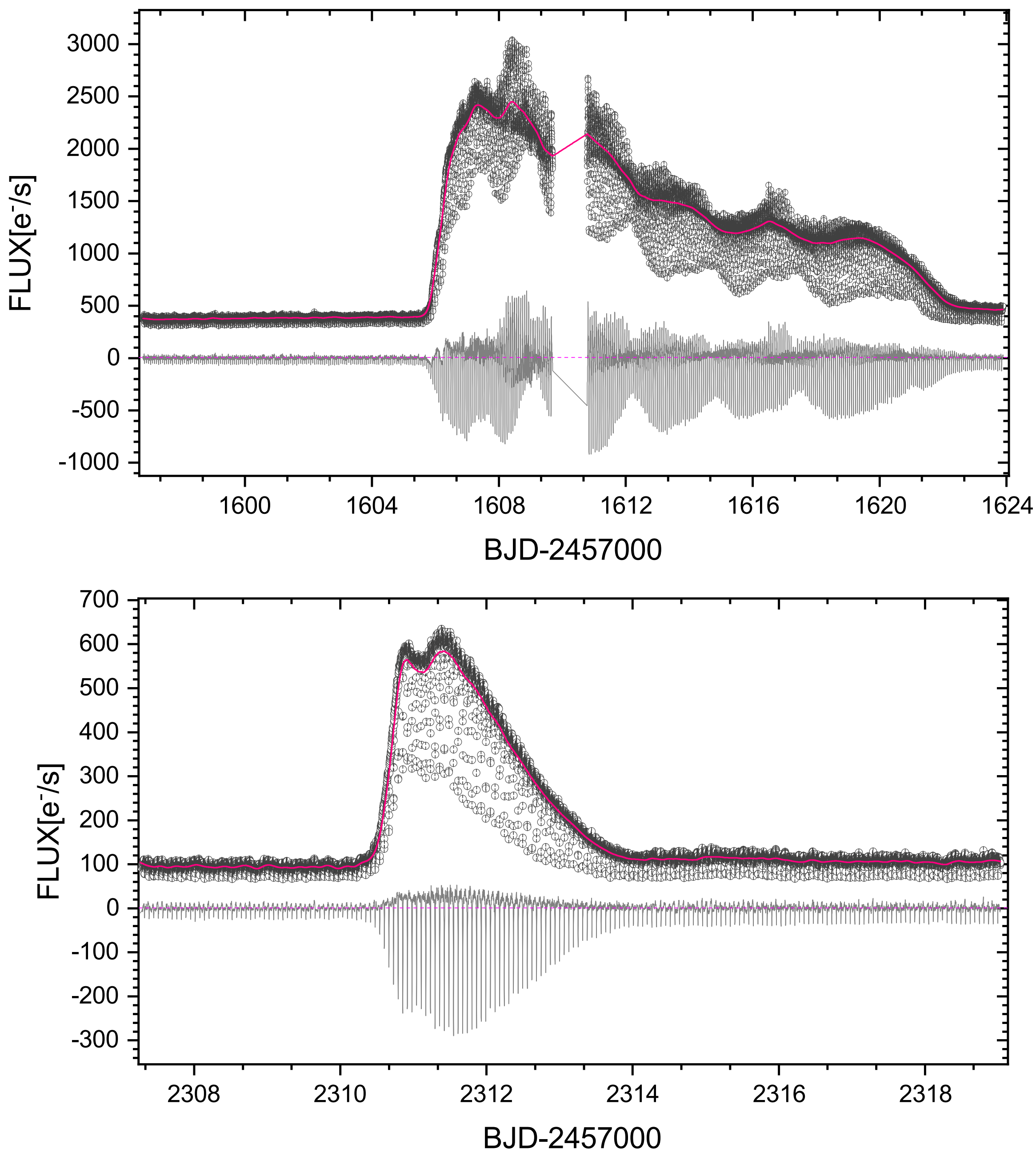

Figure 3. TESS light curve of OY Car, displaying a superoutburst in the top panel and a normal outburst in the bottom panel, as well as clear eclipse features. The red solid line represents the smoothed light curve using the LOESS fit. The gray line is the detrended light curve by subtracting the smoothed light curve.

eclipses. Figure 3 shows a superoutburst starting on BJD 2458605 and a normal outburst starting on BJD 2459310. There is a significant change in depth and shape during the outburst cycle. To measure the depth, width, and time of the minimum light of the eclipses, we performed Gaussian fits on all eclipse curves and visually checked whether each fit was reasonable. The width was approximated by calculating the full width at half-minimum (FWHM) for each fit through numerical methods. This method allowed us to identify any outliers or erroneous data points, ensuring the reliability of our results. We define the eclipse depth as the difference between the average out-of-eclipse flux and the minimum flux of the eclipses. This method is effective and well used for quiescent data and normal outbursts, but there is a significant uncertainty when the superhump appears. We also performed an $O-C$ analysis for all times of the minimum to study the eclipse variations during outburst and superoutburst. The $O-C$ values are calculated by using a new initial epoch, BJD 2458596.83097 for the superoutburst and BJD 2459307.32021 for the normal outburst. These parameters are plotted in Figures 5 and 6. We discuss these variations in Section 4.2.

To study how the periodic signals varied as a function of time, we constructed two weighted wavelet Z-transform (WWZ) power spectra from the detrended TESS light curves by using the VARTOOLS program (J. D. Hartman & G. Á. Bakos 2016), as shown in the second panel of Figures 5 and 6. A frequency step of $0.1/T$ is used to calculate the WWZ transform up to a maximum frequency of 100 day^{-1}, where T is the time baseline of the light curve. In our analysis, we employ a time-shift step of 0.1 day to account for time-

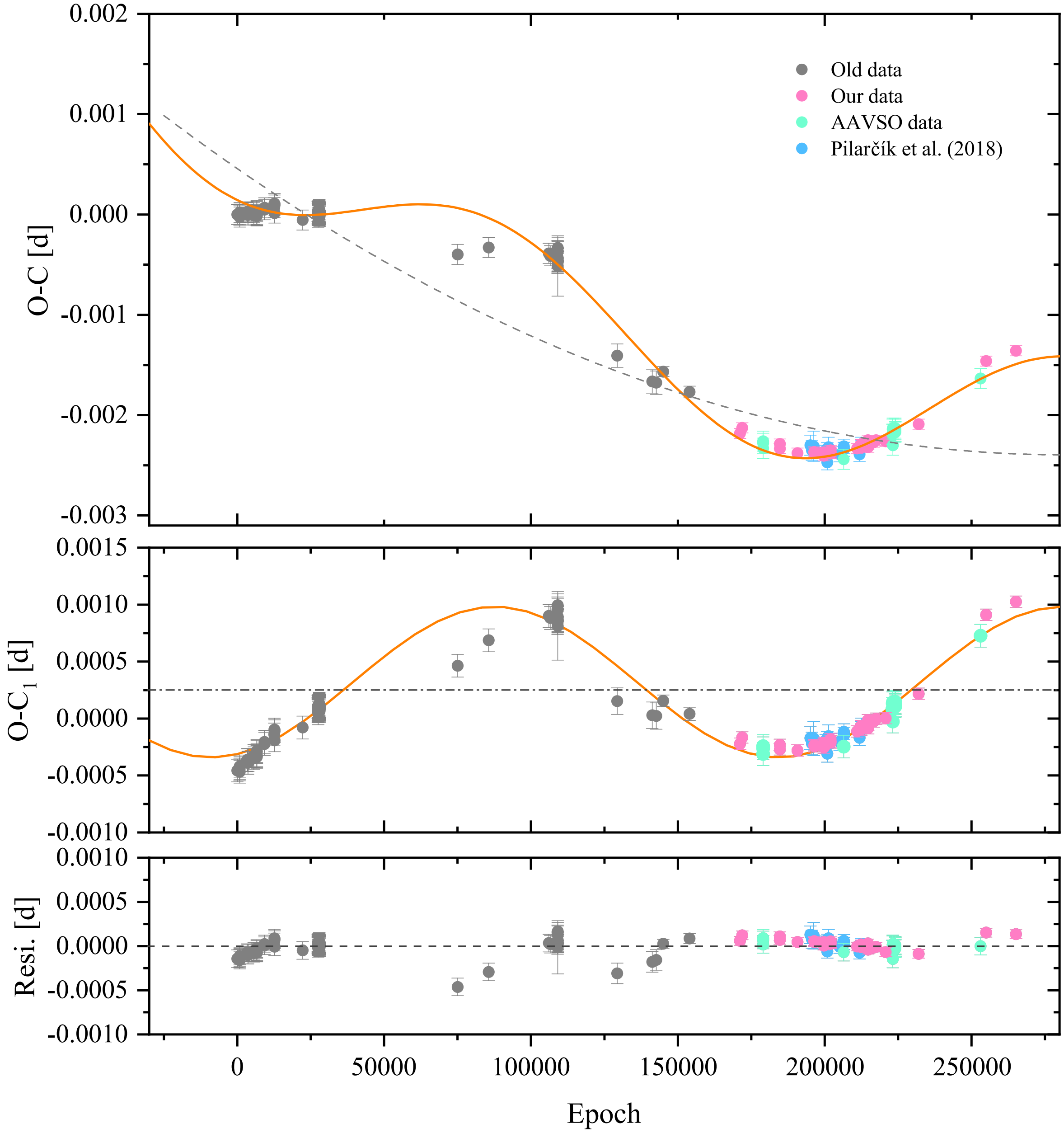

Figure 4. Updated $O-C$ diagram of OY Car constructed with a quadratic plus the sinusoidal ephemeris. The gray and light cyan points denote the historical timings, while the hot pink points refer to our eclipse timings, and the mint green points denote the AAVSO data. The orange solid line and gray dashed line in the top panel represent the best-fit model and the quadratic term of the model, respectively. The middle panel shows the LTTE orbit, and the bottom panel displays the fit residuals from the full ephemeris.

shifts spanning from the first to the last observation. In Figure 5, the power was concentrated around the orbital period and its second harmonic. The second harmonic signal is stronger than the orbital period during quiescence. At the outset of the outburst, the second harmonic quickly disappeared, and the orbital period returned to dominate, implying that this harmonic originates from the interaction of eclipses and orbital humps. The power begins to oscillate, and the power spectrum shows distinct higher harmonics after the superhump appears. Moreover, there is a quasiperiodic signal with a frequency of $\sim$3.49 day^{-1} from BJD 2458599.44 to BJD 2458601.77. We suggest that the variable in the mass transfer rate could be the cause of this signal. In Figure 6, the power was strongest at the orbital period and its second harmonic throughout the full light curve. This harmonic rapidly weakened during normal outbursts, indicating that the orbital humps in outbursts become weaker and disappear at maximum.

4. Discussion

4.1. Orbital Period Variations

4.1.1. Possible Interpretation of Long-term Period Increase

The upward parabolic variation in Figure 4 reveals a continuous increase at a rate of $+5.70 \times 10^{-13}$ s s^{-1}. OY Car is a short-period CV below the period gap. The evolution of short-period CVs is driven by angular momentum losses associated with the emission of gravitational radiation, resulting in their orbital period decrease (e.g.,

Table 2
Orbital Parameters of the Circumbinary Giant Planet in OY Car

Parameters	Quadratic *plus* Sinusoidal Model	Unit
Revised epoch, ΔT_0	$+7.76(\pm 0.63) \times 10^{-4}$	days
Revised orbital period, ΔP_0	$-2.03(\pm 0.16) \times 10^{-8}$	days
Rate of the linear period increase, β	$+3.60(\pm 0.65) \times 10^{-14}$	days/cycle
The semi-amplitude, K	$6.61(\pm 0.10) \times 10^{-4}$	days
Orbital period of the third body, P_3	33.41(±0.06)	yr
Orbital phase of the third body, φ	73.34(±3.95)	deg
Projected semimajor axis, $a_{12} \sin i'$	0.114(±0.002)	au
Mass function, $f(m)$	$1.35(\pm 0.06) \times 10^{-6}$	$M_\odot$
Mass of the third body, $M_3 \sin i'$	0.011(±0.003)	$M_\odot$
Orbital radius of the third body, d_3 ($i' = 90°$)	12.13(±0.36)	au
RSS	9.77×10^{-7}	…
Adjust R-squared, R^2	0.95	…

C. Knigge et al. 2011). Therefore, the observed period increase is not consistent with the secular decrease predicted by the CV evolutionary theory. One possibility is that this increase is caused by mass transfer from the less massive star onto the more massive one. According to the evolution equation for the orbital period of the system (E. L. Robinson et al. 1991)

$$\frac{\dot{P}_{\rm orb}}{P_{\rm orb}} = \frac{3\zeta - 1}{2}\frac{\dot{M}_2}{M_2}, \tag{3}$$

the required mass transfer rate can be estimated. ζ is the mass–radius index, and the orbital period increases for $\zeta < 1/3$. The orbital period of OY Car corresponds to a mass–radius index of $\zeta = 0.643$ in the revised model from C. Knigge et al. (2011). In this case, the required mass transfer rate to produce this increase is estimated to be $\dot{M}_2 \sim 10^{-9} M_\odot$ yr^{-1}, which is at least 3 orders of magnitude higher than the published values in OY Car (e.g., J. H. Wood 1990; D. Pandel et al. 2005). Therefore, the mass transfer between the white dwarf and the donor star cannot be the reason for the long-term increase. The second possibility is that OY Car has evolved into a period bouncer, and the donor has become a substellar object. However, recent studies indicated that OY Car has a donor mass of $M_2 = 0.093 M_\odot$ above the hydrogen burning limit ($M_{\rm H} = 0.063 M_\odot$ for CVs, M. McAllister et al. 2019) and is therefore not likely to be a period bouncer. The most likely explanation for this change is that it is only a part of another longer and more complicated orbital period variation. More data are needed to check this possibility in the future.

4.1.2. Presence of a Third Body in OY Car?

Cyclic oscillations of the orbital period observed in CVs can be explained in general by the magnetic activity cycle in donors (i.e., Applegate mechanism, J. H. Applegate 1992), or the coupling of the spin of the active component with the orbital motion of the binary (so-called Applegate–Lanza mechanism, A. F. Lanza 2020), and the LTTE via the presence of a potential third body. For OY Car, we first use the model refined by C. S. Brinkworth et al. (2006) to calculate the energy requirement in the framework of the Applegate mechanism. The result found that OY Car requires more than 50% of the available energy in a full cycle ($\Delta E/E_{\rm sec} = 0.52$). During the analysis, we adopted the system parameters from M. McAllister et al. (2019) and the fitting parameters listed in Table 2. The donor luminosity can be calculated by $L_2 = \left(\frac{R_2}{R_\odot}\right)^2 \left(\frac{T_2}{T_\odot}\right)^4 L_\odot$, in which $T_2 = 2805$ K for $M_2 = 0.093 M_\odot$. An improved model from M. Völschow et al. (2016) has also been used to estimate the energy required to effect this change. The result, with the online calculator,[9] shows that the minimum required energy divided by the available energy, $\Delta E/E_{\rm sec} = 0.45$. Overall, these results indicate that OY Car needs at least about half of the available energy to drive the Applegate mechanism. These authors also suggested that the low-mass systems with a donor mass of $0.30-0.36 M_\odot$ are the most promising Applegate candidates (see M. Völschow et al. 2018). T. Ak et al. (2001) investigated the solar-type activity cycle of CV donors and found that the peak of the cycle periods is about 9.7 yr. Taken together, these results suggest that the best explanation for the cyclic modulation is probably not the magnetic activity.

We also try to assess whether the spin–orbit coupling model is the cause of this change. Combining the A. F. Lanza (2020) approximation for the relative amplitude of the variation of the angular velocity

$$\frac{\Delta\Omega}{\Omega} = -\frac{m r_0^2}{3 I_s}\frac{\Delta P}{P}, \tag{4}$$

with the rotational energy change equation yields the relationship

$$\Delta E_{\rm rot} = -[m r_0^2 \Omega^2]\frac{\Delta t}{3T}, \tag{5}$$

where m is the reduced mass of the binary, $\Delta t/T = \Delta P/P$ is the amplitude of the period modulation, r_0 is the orbital radius of the active star and usually equal to its semimajor axis length. For OY Car, the relative amplitude $\Delta P/P \approx 3.27 \times 10^{-7}$, the reduced mass is $m = \frac{M_1 M_2}{M_1 + M_2} = 0.084 M_\odot$, and the angular velocity of the donor star is $\Omega = 2\pi/P_{\rm orb} = 1.15 \times 10^{-3}$ s^{-1} due to the synchronous rotation of the system. Typically, the orbital radius corresponds to the secondary star's semimajor axis length ($r_0 = a_2 = 0.60 R_\odot$). As a result, the rotational energy change of the active star is $\Delta E_{\rm rot} \approx -6.75 \times 10^{33}$ J with a luminosity timescale of $\Delta E_{\rm rot}/L_2 = 516.8$ yr, much longer than the

[9] http://theory-starformation-group.cl/applegate/

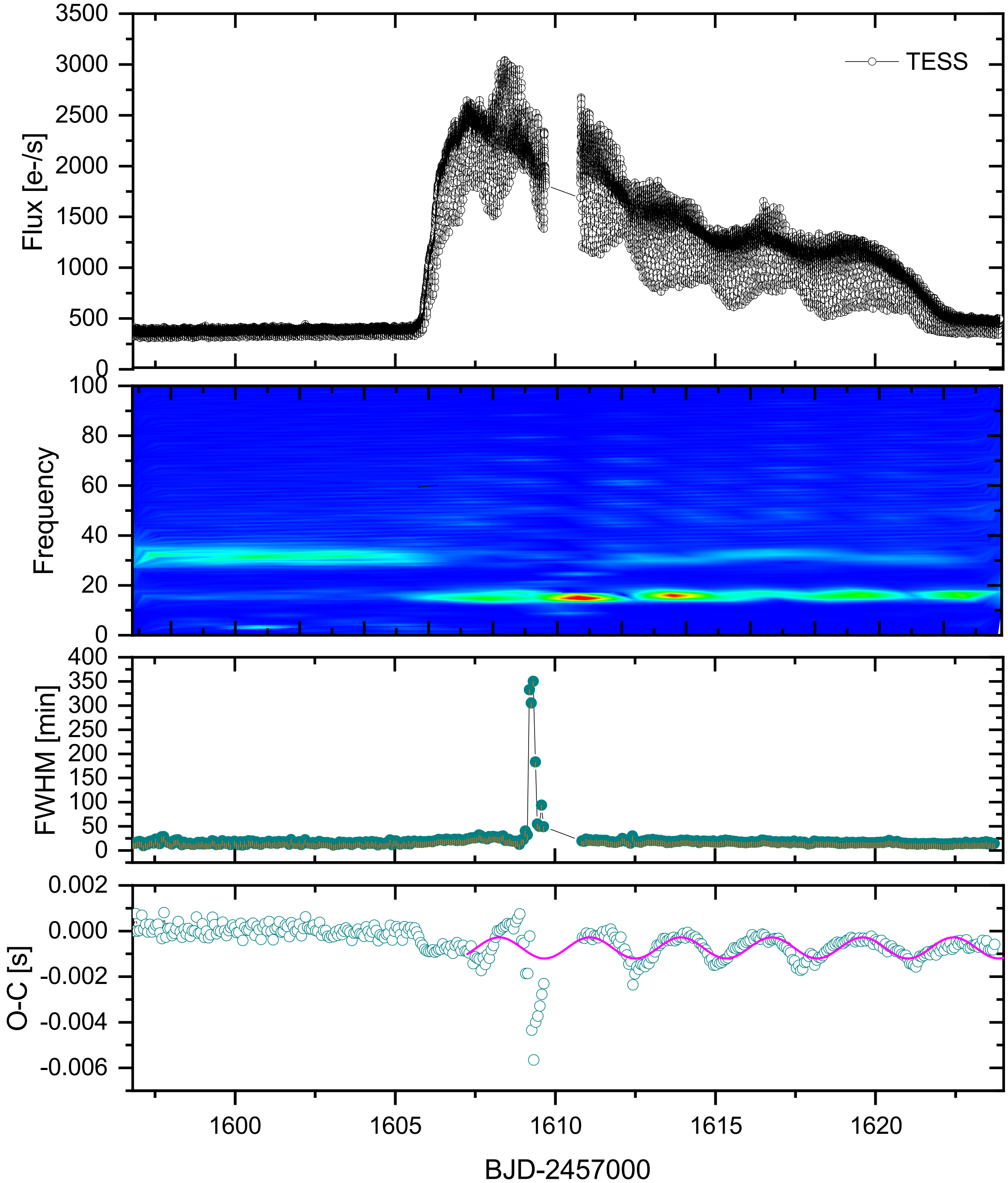

Figure 5. Top panel: the full TESS light curve of OY Car during superoutburst. From top to bottom, the remaining three panels show the WWZ around the orbital period's fundamental harmonic, the eclipse FWHM, and the eclipse $O-C$ curve. The magenta line in the bottom panel represents the best-fitting sinusoid to the eclipse $O-C$ during superoutburst.

modulation cycle. This means that even if the rotational energy dissipation during the operation of the mechanism is only 10%, the very feeble active star does not appear capable of supplying the required energy along one cycle of the modulation. The results support the idea that the magnetic activity may not be the dominant mechanism in the case of OY Car.

A more likely explanation would be the presence of a third body, leading to an LTTE on the eclipse light curves. The projected semimajor axis of the eclipsing pair orbiting the barycenter of the triple system is related to the semi-amplitude of the cyclic variation (K) by the equation:

$$a_{12} \sin i' = K \times c, \tag{6}$$

where c is the speed of light and i' is the orbital inclination of the third body. Consequently, the mass function $f(m)$ for the third body can be computed using Kepler's third law:

$$f(m) = \frac{4\pi^2}{GP_3^2} \times (a_{12} \sin i')^2 = \frac{(M_3 \sin i')^3}{(M_1 + M_2 + M_3)^2}, \tag{7}$$

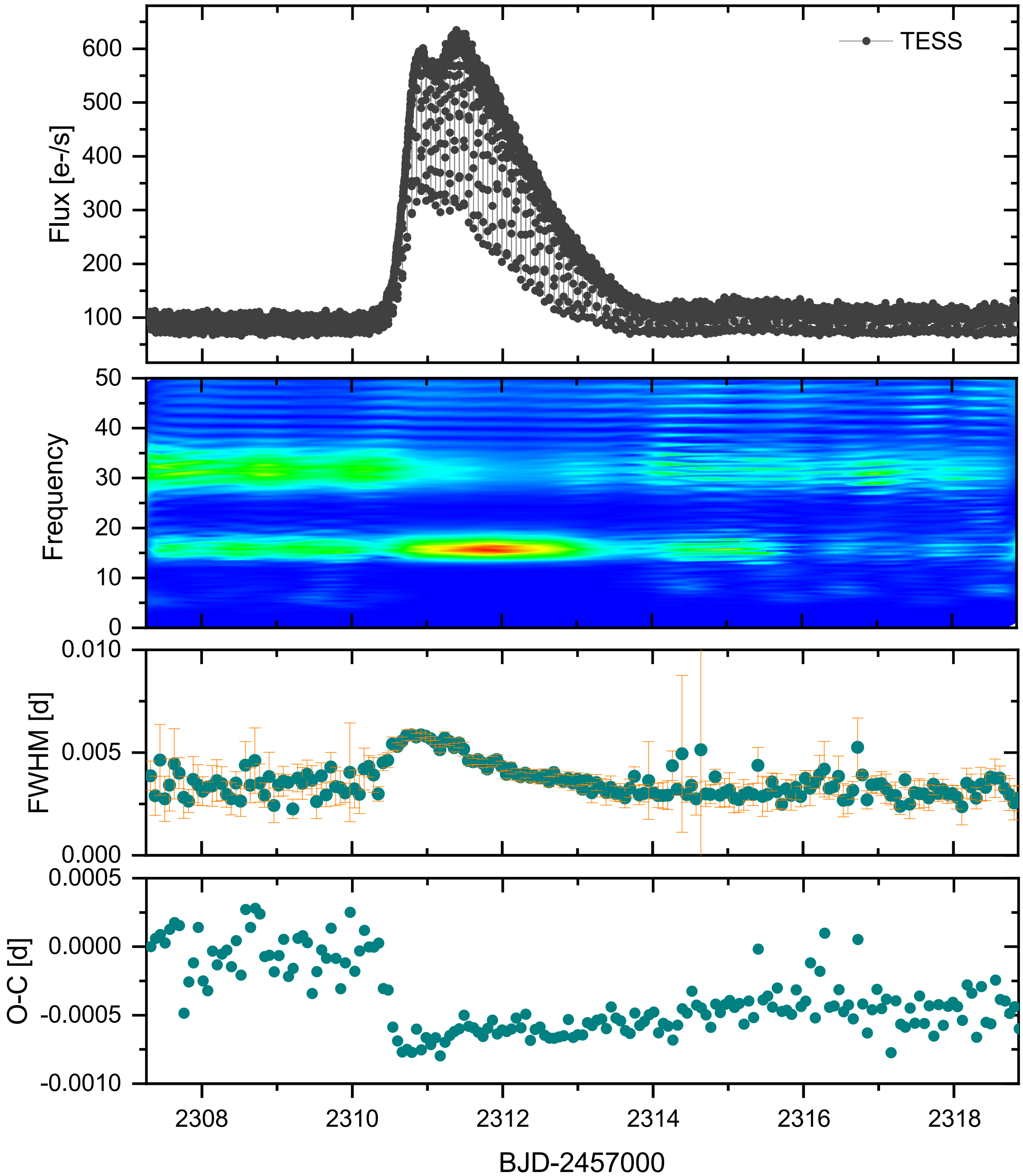

Figure 6. Top panel: the full TESS light curve of OY Car during outburst. From top to bottom, the remaining three panels show the WWZ around the orbital period's fundamental harmonic, the eclipse FWHM, and the eclipse $O-C$ curve.

where G is the gravitational constant, P_3 is the period of the cyclic oscillation, and M_1, M_2, and M_3 correspond to the masses of the white dwarf, the donor star, and the third body, respectively. With the binary parameters (M_1 and M_2) derived by M. McAllister et al. (2019) and the fitting parameters (K and P_3) listed in Table 2, we estimated the mass of the third body as $M_3 \sin i' = 0.011(\pm 0.003) M_\odot = 11.5(\pm 3.1) M_{\rm Jup}$ based on the fitting results listed in Table 2 and the mass of the two components of the binary. Considering the most likely scenario where the third body and the binary are coplanar, then its mass would match a giant planet in a circular orbit of a radius of 12.13($\pm$0.36) au. However, the residuals in Figure 4 seem to show a lower-amplitude quasiperiodic modulation, implying that the magnetic activity still contributes to the orbital period variations. Consequently, the observed period variations in OY Car should be the result of the combined action of multiple mechanisms.

4.1.3. Comparison with Previous Works

Here, we compare our results with previous studies on the orbital period variations of OY Car, including those of J. G. Greenhill et al. (2006), Z.-T. Han et al. (2015), L. Pilarčík et al. (2018), and B. E. Schaefer (2024). Note that we have not compared our work with the conclusions of several pre-2006 studies, as their analyses typically reported no significant long-term period changes in OY Car. Nevertheless, the eclipse timings reported in those papers were essential and have been incorporated into our analysis to ensure a sufficiently long data baseline.

Our analysis yields orbital parameters that differ from some previous studies, most notably the recent work by B. E. Schaefer (2024) and our earlier study in Z.-T. Han et al. (2015). B. E. Schaefer (2024) argued that the $O-C$ variations of OY Car are best described by a six-segment broken line rather than a smooth cyclic modulation, suggesting abrupt period changes potentially associated with nova eruptions or unknown mechanisms. However, that analysis excluded a significant portion of historical data (e.g., measurements from Z.-T. Han et al. 2015) due to concerns over timing measurement inconsistencies. In this work, we have addressed these concerns by redetermining all eclipse times from 2008 to 2025 using the derivative method (J. H. Wood et al. 1985) to ensure homogeneity with the historical dataset. By combining these recalibrated timings with all available reliable historical data, we present the most comprehensive $O-C$ diagram to date. As shown in Figure 4, the high-cadence coverage between Epochs 100,000 and 265,000 reveals a clearly continuous and smooth variation. There is no evidence of the sudden jumps or sharp breaks required by a segmented line model; conversely, the data strongly favor a smooth evolution well described by a superposition of a quadratic trend and a sinusoidal oscillation.

Furthermore, our derived modulation period ($P_3 \approx 33.4$ yr) and the secular period increase contrast with the 14.0 yr cycle and secular period decrease reported in Z.-T. Han et al. (2015). This discrepancy is attributable to two primary factors: methodology and temporal baseline. First, Z.-T. Han et al. (2015) utilized a polynomial fitting method to determine eclipse minima, whereas earlier studies (e.g., N. Vogt et al. 1981; J. H. Wood et al. 1989) utilized the derivative method. As noted by L. Pilarčík et al. (2018), mixing these distinct methodologies introduces systematic time offsets (approximately 80 s), which can distort the $O-C$ shape and the resulting period derivative. By consistently applying the derivative method in this work, we have eliminated these systematics. Second, the dataset in Z.-T. Han et al. (2015) spanned a significantly shorter baseline. The inclusion of nearly a decade of new observations in the present study has been critical in resolving the true long-term behavior of the system. Our derived modulation period of 33.4 yr is in good agreement with the ∼35 yr cycle proposed by J. G. Greenhill et al. (2006) and the 29 yr cycle found by L. Pilarčík et al. (2018), suggesting that the earlier 14 yr solution was likely an artifact of insufficient coverage. Similarly, the change in the sign of the secular trend from the decrease reported in earlier short-baseline studies to the increase found here demonstrates that limited temporal coverage can lead to the misinterpretation of a segment of a long-period oscillation as a secular trend.

4.2. Outburst Properties of OY Car

4.2.1. Eclipse Depth Evolution and Hysteresis

Recent studies of eclipsing dwarf novae have established that, during quiescence, the eclipse depth is typically linearly correlated with the out-of-eclipse flux (e.g., P. J. Groot et al. 1998; S. Scaringi et al. 2013; J. M. C. Court et al. 2019, 2020; Z.-T. Han et al. 2021). A slope of unity in this relation defines the "line of maximal eclipse," implying that a constant fraction of the accretion disk is obscured during each eclipse. Deviations from this line during outbursts manifest as hysteresis loops, tracing the evolution of the disk's radius and temperature profile. We applied this analysis to the TESS observations of OY Car. Figures 7 and 8 display the relationship between eclipse depth and out-of-eclipse flux for the superoutburst and the normal outburst, respectively. For the quiescent data preceding the superoutburst, a linear fit yields a slope of $m = 0.56 \pm 0.05$. For the data surrounding the normal outburst, the fit yields a slope of $m = 0.87 \pm 0.02$. Unlike the results for Z Cha in J. M. C. Court et al. (2019), where the quiescent slope was consistent with unity, our derived slopes deviate significantly from $m = 1$. This suggests that the geometry of the eclipse—specifically the fraction of the disk flux being occulted—was not constant even during the quiescent phases analyzed here. This deviation likely points to structural changes in the accretion disk, such as variations in the radial-temperature gradient or disk radius, occurring prior to the onset of the outbursts.

Because the observed slopes deviate from unity, and given the large pixel scale of TESS (∼21″ pixel^{-1}), which can introduce background blending uncertainties, the y-intercepts of these fits yield unphysical negative fluxes (e.g., $-72\,e^{-1}\,\mathrm{s}^{-1}$ for the normal outburst). Consequently, we do not attempt to derive the absolute flux of the donor star from these intercepts. Instead, we focus on the relative morphological evolution of the outbursts. As the system enters an outburst, the data points depart rapidly from the quiescent trend, forming distinct hysteresis loops. In the case of the normal outburst (Figure 8), the trajectory traces a counterclockwise loop. According to the models by J. M. C. Court et al. (2019), the direction and shape of this hysteresis indicate the relative timing of changes in the disk radius versus the mass accretion rate. The observed loops confirm that the accretion disk expands significantly during the outburst, altering the fraction of the disk that is eclipsed by the secondary star. The complex hysteresis seen during the superoutburst (Figure 7) reflects the more intricate interplay between the thermal instability and the tidal instability driving the superhump modulation.

4.2.2. Normal Outburst

The normal outburst curve of OY Car is shown in Figure 6. Throughout the outburst, the depth, shape, and FWHM value of the eclipses show distinct variations, indicating that the disk radius and the radial-temperature gradient variations. The mid-eclipse brightness during outburst is also constantly changing. Therefore, the disk is not entirely eclipsed by the donor star. To demonstrate this, we can perform the following calculation by comparing the donor star radius to the circularization radius of the disk, which can be obtained from (J. Frank et al. 2002)

$$\frac{R_{\mathrm{circ}}}{a} = (1 + q)(0.5 - 0.277 \log q)^4 , \quad (8)$$

where a represents the orbital separation and q is the mass ratio. Applying the binary parameters from M. McAllister et al. (2019), we derived the smallest radius of the accretion disk $R_{\mathrm{circ}} \sim 0.20 R_{\odot}$. This value is significantly greater than the donor's radius of $\sim 0.14 R_{\odot}$, implying that the accretion disk is always partially visible, even in quiescence. Our analysis

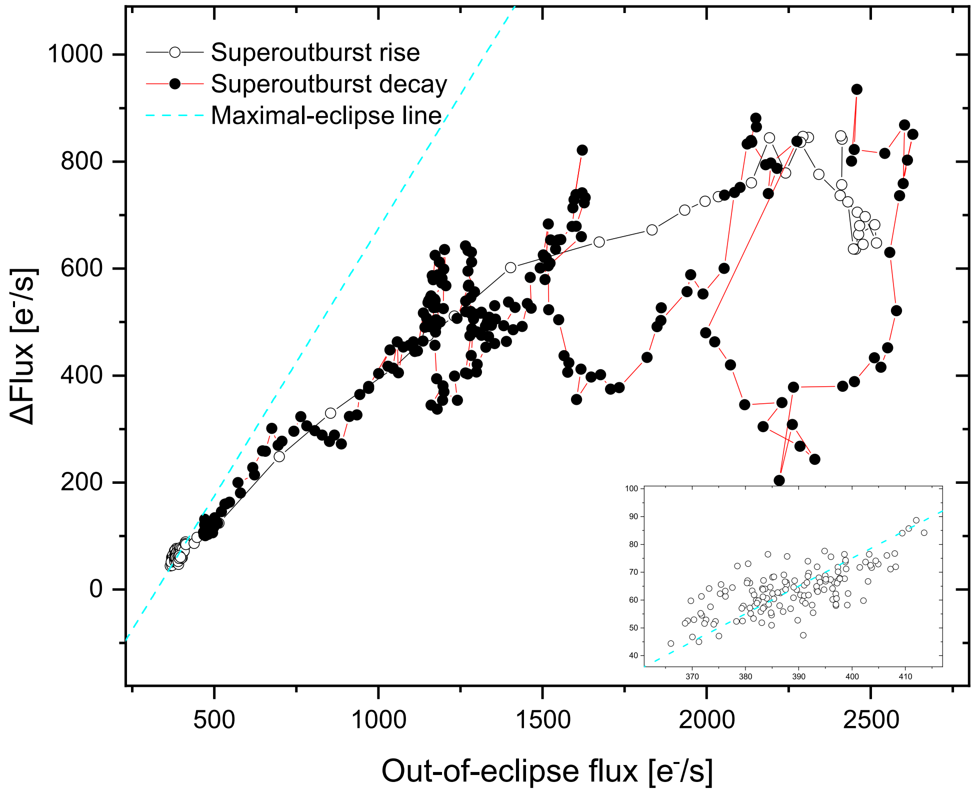

Figure 7. Relationship between the eclipse depth and the out-of-eclipse flux during superoutburst for all well-constrained eclipses in the TESS data of OY Car. The open solid circles denote the cycles during quiescence and outburst rise, and the solid circles represent the outburst decline. The cyan dashed line represents the line of maximal eclipse by fitting a linear equation with the gradient = 1 to the quiescent data. The inset shows a zoom-in of the eclipses used to calculate this line.

yields a near 1:1 relationship between eclipse depth and the out-of-eclipse flux during the quiescent period before and after the normal outburst (the slope m = 0.87). This relation corresponds to the so-called "line of maximal eclipse," in which the same part of the disk is eclipsed during each cycle (S. Scaringi et al. 2013). When we set the slope to 1, the intercept value of $-71.9\, e^{-}\,\mathrm{s}^{-1}$ can be used as a rough estimate of the donor's flux. At the onset of the outburst, the data points rapidly deviate from the "line of maximal eclipse" and produce a clear hysteretic loop that consists of rise and decay branches (see Figure 8). This implies the accretion disk expands during outburst to become larger than during quiescence.

The normal outburst of OY Car is a typical outside-in outburst (i.e., Type A), which has a rapid rise and a slower decay. The eclipse FWHM values are nearly maximal at the time of the outburst peak, supporting that the outburst initiated in the outer disk and propagated inward. An outburst originating in the outer disk leads to an immediate increase in eclipse width, as the donor star is unable to fully obscure the entire outbursting region. The mid-eclipse times during outburst were observed to occur up to a few minutes earlier compared to quiescence (see $O-C$ curve in Figure 6). This timing shift is likely attributable to a reduced relative contribution from the hot spot to the system's total flux during the outburst. Since the hot spot is typically eclipsed after the central regions of the accretion disk, its diminished presence leads to an earlier observed eclipse minimum. In contrast, during quiescence, the hot spot contributes significantly to the light curve, resulting in a delayed eclipse minimum. During outbursts, the disk's increased brightness compared to quiescence leads to its emission centroid being eclipsed earlier (G. Ramsay et al. 2017).

4.2.3. Superoutburst

In Figure 7, our analysis failed to produce a well-defined 1:1 correlation to eclipse depth and out-of-eclipse flux prior to the superoutburst onset (the slope $m = 0.56$). This implies that the quiescent disk's radius before the superoutburst was larger compared to the quiescent disk's radius during the periods surrounding normal outbursts. The result supports the tidal thermal instability (TTI) framework for superoutbursts (Y. Osaki 1989), which suggests that each normal outburst removes less material from the disk compared to what has been added, causing a gradual increase in mass and size. Around BJD 2458605.75, OY Car generated a precursor normal outburst (a normal outburst that immediately precedes and triggers the superoutburst). Just after the precursor's peak, a decline in the eclipse FWHM and an increase in its depth were observed, precisely mirroring the behavior seen in another normal outburst (Figure 6). At BJD $\sim$ 2458607.97, the appearance of the first superhump marked the immediate rise of the light curve to superoutburst maximum. Following the superoutburst peak, the superhump begins to fade, and its interaction with eclipses makes the light curve very complicated. The fade was observed to be centered on the coincidence of eclipse minima with superhump maxima. At this time, the eclipse FWHM begins to increase suddenly, until the superhump moves to a phase of $\sim$0.25 and then returns to the baseline (third panel in Figure 5). This indicates that the superhump fade is strongly dependent on the orbital phase.

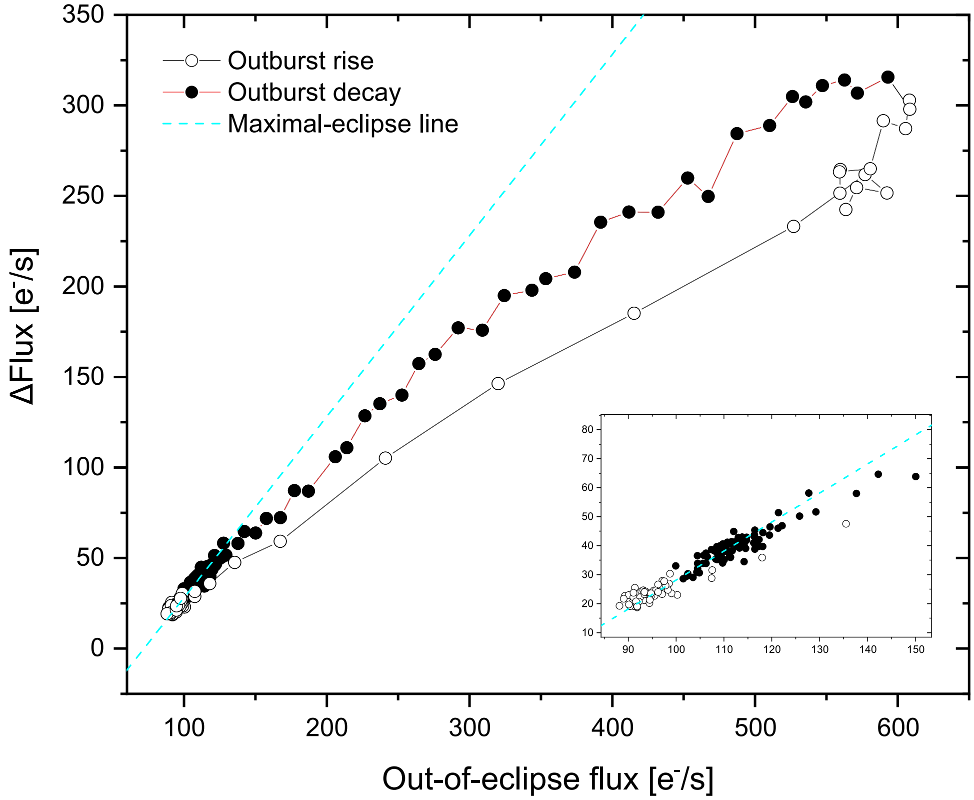

Figure 8. Relationship between the eclipse depth and the out-of-eclipse flux during normal outburst for all well-constrained eclipses in the TESS data of OY Car. The open solid circles denote the cycles during quiescence and outburst rise, and the solid circles represent the outburst decline. The cyan dashed line represents the "line of maximal eclipse" by fitting a linear equation with the gradient = 1 to the quiescent data. The inset shows a zoom-in of the eclipses used to calculate this line.

There are two possible explanations for this phenomenon. One is that a part of the superhump light originates from the disk's vertically extended rim, whose edge-on visibility varies across the orbital cycle (Y. Osaki & F. Meyer 2003). An alternative hypothesis is the obscuration of the inner disk by vertically extended disk structure at specific orbital phases (I. Billington et al. 1996; J. R. Murray 1998).

During the superoutburst, the eclipse $O-C$ curve showed a clear quasiperiodic oscillation (Figure 5). During the period of dramatic eclipse FWHM variation, the eclipse $O-C$ timings also exhibited abrupt changes, implying that the origin of both changes should be the same. While the quasiperiodic variation provides strong evidence for the presence of an eccentric precessing disk in OY Car. In fact, previous authors have tried to find the eccentric disk in OY Car by the $O-C$ eclipse timings during the superoutburst (W. Krzeminski & N. Vogt 1985), but a later study by T. Naylor et al. (1987) indicated that the $O-C$ modulation showed reduced significance relative to earlier expectations due to a lack of data. F. V. Hessman et al. (1992) deduced the existence of an eccentric disk by analyzing variations in hot spot eclipse ingress times and the trajectory of the accretion stream. To obtain the precessional period of the disk, we fit a sine function to the quasiperiodic variation, and the best-fit model was displayed in the bottom panel of Figure 5 (magenta solid line). The best-fitting parameters are listed in Table 3. The result reveals a mean precessional period of the disk of 2.84 ($\pm$0.02) days. We acknowledge that the precession period likely varies throughout the superoutburst due to the evolution of the disk radius, as suggested by the residuals in the $O-C$ diagram and the superhump evolution itself. However, extracting this characteristic mean precession period is essential. It allows us to independently verify the superhump period via the beat frequency relation (Equation (10)) and provides a crucial parameter for estimating the binary mass ratio in the subsequent analysis (see Section 4.3). The interaction between the precessional period and the orbital cycle would subsequently manifest as the superhump periodicity, which will be discussed in the next section.

Table 3
Sinusoidal Fit Parameters to the $O-C$ Diagram during Superoutburst

Sine Fitting:		
$(O-C)' = \Delta T_0' + K' \sin(\frac{\pi}{\omega} \times T' - \frac{\pi}{\omega} \times T_C')$		
Parameters	Value	Error
$\Delta T_0'$	7.41×10^{-4}	2.09×10^{-5}
K'	4.62×10^{-4}	2.93×10^{-5}
ω	1.42	0.01
T_C'	−154.86	13.87
RSSs	8.85×10^{-8}	⋯
Reduced R-square	0.55	⋯

4.3. Superhump Period and Evolution in OY Car

While previous photometric studies have reported various superhump periods for OY Car (e.g., W. Krzeminski & N. Vogt 1985; R. Schoembs 1986), the high-cadence TESS data enable a detailed resolution of the superhump evolution. A direct measurement from the TESS light curve during the growing phase (stage A) yields a period of $P_{SH} \approx 0.0647$ day.

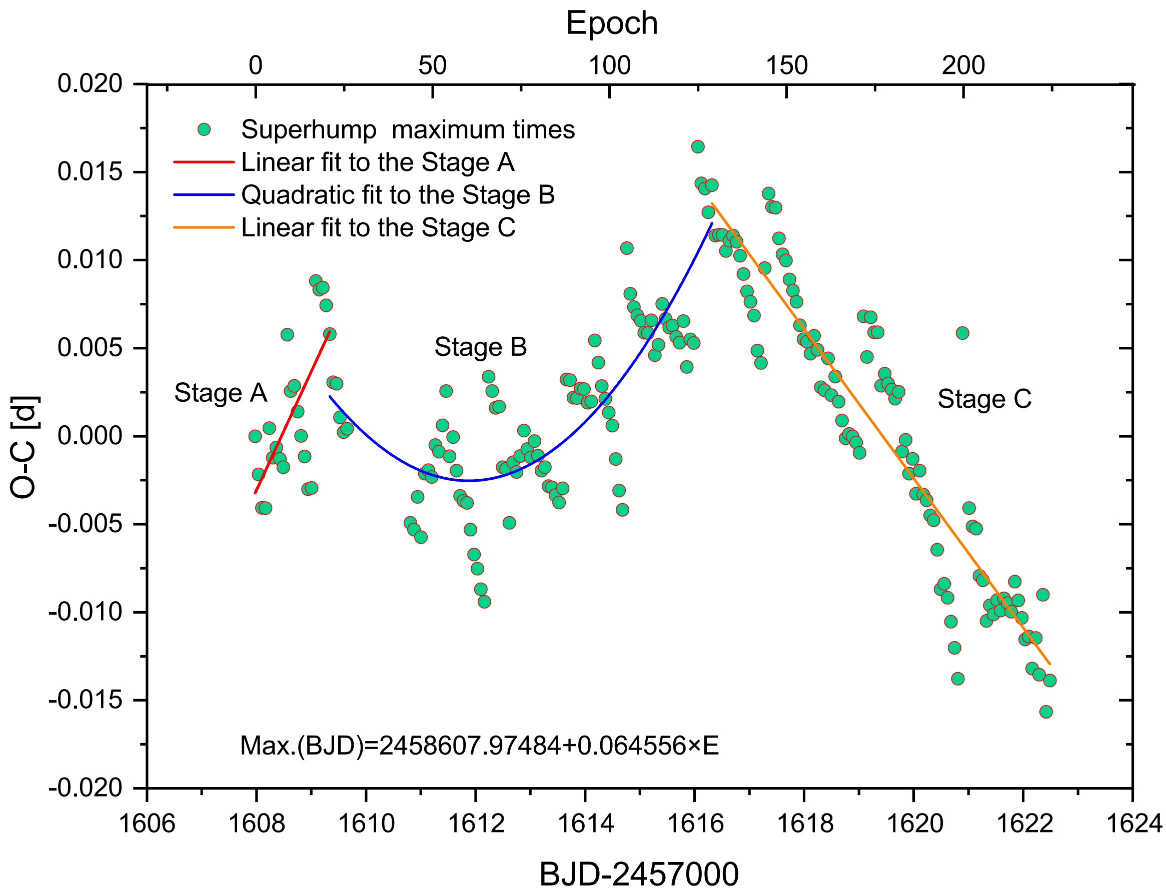

Figure 9. The $O-C$ diagram of superhump maximum times, showing three distinct stages (A, B, and C). The red and orange solid lines are the linear fit to the data in stages A and C, respectively. The blue solid line is a quadratic ephemeris fit to the superhumps in stage B. The upward parabola reveals that the superhump period derivative is positive during this stage.

As discussed below, this value is critical for the dynamical estimation of the mass ratio. However, applying empirical mass ratio relations (e.g., C. Knigge 2006) requires a characteristic mean superhump period, typically corresponding to the stabilized stage B. We independently derive this mean period using the precession period ($P_{\rm prec} = 2.84(\pm0.02)$ days) obtained from our eclipse $O-C$ analysis (Section 4.2.3). Via the beat frequency relation:

$$\frac{1}{P_{\rm sh}} = \frac{1}{P_{\rm orb}} - \frac{1}{P_{\rm prec}}, \qquad (9)$$

we calculate a mean superhump period of $P_{\rm sh} = 0.06456$ day. This value, distinct from the stage A period, is consistent with the stabilized period observed during stage B (see Figure 9).

With both the stage A period and the mean (stage B) period established, we proceed to estimate the binary mass ratio (q) using two independent methods to probe the disk dynamics. Using the measured $P_{\rm SH} \approx 0.0647$ day, we calculated the precession rate $\epsilon^* = 1 - P_{\rm orb}/P_{\rm SH}$ and substituted it into the dynamical relation (Equation (5) in T. Kato & Y. Osaki 2013):

$$q(\epsilon^*) = -0.0016 + 2.60\epsilon^* + 3.33(\epsilon^*)^2 + 79.0(\epsilon^*)^3. \qquad (10)$$

This yields $q \approx 0.0658$, which is significantly smaller than the robust eclipse-modeling value of $q = 0.1065$ (M. McAllister et al. 2019). Such discrepancies are not unique to OY Car but are common among deeply eclipsing SU UMa systems. As documented by T. Kato & Y. Osaki (2013), similar underestimations of q have been observed in systems like HT Cas, DV UMa, and XZ Eri. In these high-inclination binaries, the deep eclipses superimpose on the superhump modulations, often distorting or masking the maxima during the short-lived (1–2 days) stage A phase. This interference makes the reliable isolation of the pure stage A period intrinsically difficult, leading to measurements that likely reflect the early stage B period. In stage B, "pressure effects" within the disk reduce the precession rate relative to the purely dynamical value, resulting in a systematically lower derived q (T. Kato 2022). To test this hypothesis, we applied the empirical relation from C. Knigge (2006), which is calibrated primarily using superhumps in the plateau phase (stage B) and thus implicitly accounts for pressure effects. Using the average superhump period ($P_{\rm sh} = 0.06456$ day) and measured superhump period excess ($\epsilon = 0.0227$), the empirical relation

$$q = (0.114 \pm 0.005) + (3.97 \pm 0.41) \times (\epsilon - 0.025), \qquad (11)$$

yields a mass ratio of $q = 0.1049(\pm0.0051)$. This value is in excellent agreement with the eclipse-modeling result ($q = 0.1065$). The success of the empirical relation (calibrated for stage B) contrasted with the underestimation of the dynamical method (valid only for the pure stage A) provides compelling evidence that the superhumps observed in OY Car are strongly influenced by pressure effects. Consequently, we adopt the eclipse-modeling mass ratio as the definitive parameter.

In fact, the superhump period varies with time during superoutburst. To explore the superhump period drifts in OY Car, we conducted an $O-C$ analysis by fitting polynomials to the superhump maxima and determining their maximum times. The observed times of maxima were compared with those predicted by a linear ephemeris adopting our estimate of superhump period. The result is plotted in Figure 9 and shows three distinct stages: A, B, and C. Stage A is an initial growing stage with a longer superhump period; during stage B, the superhump period increases smoothly over time with a positive period derivative $\dot{P}$; stage C shows a shorter, almost constant period. The positive $\dot{P}$ for stage B superhumps has been reported in previous studies (T. Kato et al. 2015, 2017), but the limited observational coverage for individual superburst events suggests that the results remain inconclusive. Fortunately, TESS provides a complete and continuous superburst curve to obtain the full evolution of the superhumps (see Figure 9). A quadratic ephemeris was employed to model the $O-C$ diagram during stage B. The result reveals the superhump period derivative $\dot{P} = +9.42 \times 10^{-5}$, which is almost consistent with the result given by T. Kato et al. (2015), confirming that a positive $\dot{P}$ during stage B is reliable. The physical origins of these evolutionary stages have been updated in recent studies. Stage A superhumps correspond to the growing phase of the 3:1 resonance, reflecting the purely dynamical precession rate of the accretion disk at the resonance radius. Stage B superhumps appear after the resonance is fully established; in this stage, the precession rate is reduced by pressure effects within the disk, which can lead to the observed period variations. Finally, stage C superhumps exhibit a stable period that is typically shorter than that of stage B. While the exact origin of stage C remains an open question, T. Kato et al. (2016) proposed that the transition to stage C is related to the propagation of a cooling wave in the accretion disk, which alters the disk structure and the tidal instability condition.

5. Conclusions

We have performed a comprehensive photometric study of the eclipsing SU UMa-type dwarf nova OY Car using ground-based data and high-cadence observations from TESS. The eclipse timing analysis reveals a secular period increase superimposed with a cyclic oscillation of 33.4 yr. This modulation is most plausibly interpreted as the LTTE caused by a circumbinary giant planet with a mass of $11.5(\pm 3.1) M_{\rm Jup}$ orbiting in a circular orbit.

The TESS light curve captures one normal outburst and one superoutburst. By analyzing the relationship between eclipse depth and out-of-eclipse flux, we find distinct hysteresis loops that indicate significant disk expansion during outbursts. Notably, the quiescent slope deviates significantly from unity prior to the superoutburst. We attribute this deviation to changes in the disk structure, specifically a variation in the disk radius during the supercycle, which provides support for the TTI model.

Our analysis of the superhump evolution identifies the standard A, B, and C evolutionary stages. An $O-C$ analysis of the superhump maxima confirms a positive period derivative ($\dot{P} > 0$) during stage B. Furthermore, we find a discrepancy between the mass ratio derived from the dynamical method using the stage A period and that derived from the empirical method using the mean period from eclipse timings. This highlights the significant impact of pressure effects on the accretion disk precession.

In summary, this work underscores the complexity of the OY Car system, demonstrating that its long-term evolution and short-term outburst dynamics are driven by a combination of circumbinary companions and intrinsic disk instabilities. Continuous eclipse monitoring and high-cadence multicolor photometry during future superoutbursts will be essential to further constrain the third-body orbit and resolve the disk's structural evolution via eclipse mapping.

Acknowledgments

This work is partly supported by the Yunnan Fundamental Research Projects (grant Nos. 202301AT070299, 202401CF070039) and the Yunnan Students' Innovative Entrepreneurship Training Program (No. 202411390003) and is also supported by the Yunnan Revitalization Talent Support Program "Young Talent" Project. The authors gratefully acknowledge the computing support provided by the JRT Science Data Center at Yuxi Normal University. The new photometric observations presented here were made with the 2.15 m Jorge Sahade telescope in Argentina. Some/all of the data presented in this article were obtained from the Mikulski Archive for Space Telescopes (MAST) at the Space Telescope Science Institute. The specific observations analyzed can be accessed via doi:10.17909/sncw-6j08. Moreover, this paper includes data collected by the TESS mission, downloaded from MAST. Funding for the TESS mission is provided by the NASA Explorer Program. We also appreciate the contributions of the AAVSO database and the International Variable Star Index database (VSX[10]) in this research.

ORCID iDs

Hu-Shang Xu https://orcid.org/0000-0002-7809-0347
Ai-Jun Dong https://orcid.org/0000-0003-4151-0771

References

Ak, T., Ozkan, M. T., & Mattei, J. A. 2001, A&A, 369, 882
Applegate, J. H. 1992, ApJ, 385, 621
Baptista, R. 2016, ASSL, 439, 155
Baskill, D. S., Wheatley, P. J., & Osborne, J. P. 2005, MNRAS, 357, 626
Billington, I., Marsh, T. R., Horne, K., et al. 1996, MNRAS, 279, 1274
Bonnet-Bidaud, J. M., Motch, C., & Mouchet, M. 1985, A&A, 143, 313
Brinkworth, C. S., Marsh, T. R., Dhillon, V. S., et al. 2006, MNRAS, 365, 287
Bruch, A., Beele, D., & Baptista, R. 1996, A&A, 306, 151
Collins, K. A., Collins, K. I., Pepper, J., et al. 2018, AJ, 156, 234
Cook, M. C. 1985, MNRAS, 215, 211
Copperwheat, C. M., Marsh, T. R., Parsons, S. G., et al. 2012, MNRAS, 421, 149
Court, J. M. C., Scaringi, S., Littlefield, C., et al. 2020, MNRAS, 494, 4656
Court, J. M. C., Scaringi, S., Rappaport, S., et al. 2019, MNRAS, 488, 4149
Frank, J., King, A., & Raine, D. J. 2002, Accretion Power in Astrophysics (Cambridge Univ. Press), 54
Greenhill, J. G., Hill, K. M., Dieters, S., et al. 2006, MNRAS, 372, 1129
Groot, P. J., Augusteijn, T., Barziv, O., et al. 1998, A&A, 340, L31
Han, Z.-T., Qian, S.-B., Fernández Lajús, E., et al. 2015, NewA, 34, 1
Han, Z.-T., Qian, S.-B., Han, Q.-W., et al. 2023, ApJ, 953, 63
Han, Z.-T., Qian, S.-B., Irina, V., et al. 2017, AJ, 153, 238
Han, Z.-T., Soonthornthum, B., Qian, S.-B., et al. 2021, AJ, 162, 205
Hartman, J. D., & Bakos, G. Á. 2016, A&C, 17, 1
Harvey, D., Skillman, D. R., Patterson, J., et al. 1995, PASP, 107, 551

[10] https://vsx.aavso.org/

Hessman, F. V., Mantel, K.-H., Barwig, H., et al. 1992, A&A, 263, 147
Horne, K. 1985, MNRAS, 213, 129
Kato, T. 2022, arXiv:2201.02945
Kato, T., Hambsch, F.-J., Dubovsky, P. A., et al. 2015, PASJ, 67, 105
Kato, T., Isogai, K., Hambsch, F.-J., et al. 2017, PASJ, 69, 75
Kato, T., & Osaki, Y. 2013, PASJ, 65, 115
Kato, T., Pavlenko, E. P., Shchurova, A. V., et al. 2016, PASJ, 68, L4
Kimura, M., & Osaki, Y. 2021, PASJ, 73, 1225
Knigge, C. 2006, MNRAS, 373, 484
Knigge, C., Baraffe, I., & Patterson, J. 2011, ApJS, 194, 28
Krzeminski, W., & Vogt, N. 1985, A&A, 144, 124
Lanza, A. F. 2020, MNRAS, 491, 1820
Lasota, J.-P. 2001, NewAR, 45, 449
Mauche, C. W. 1998, ASPC, 137, 113
Mauche, C. W., & Raymond, J. C. 2000, ApJ, 541, 924
McAllister, M., Littlefair, S. P., Parsons, S. G., et al. 2019, MNRAS, 486, 5535
Montgomery, M. M. 2009, MNRAS, 394, 1897
Motch, C. 1981, A&A, 100, 277
Murray, J. R. 1998, MNRAS, 297, 323
Naylor, T., Charles, P. A., Hassall, B. J. M., et al. 1987, MNRAS, 229, 183
Osaki, Y. 1989, PASJ, 41, 1005
Osaki, Y. 1996, PASP, 108, 39
Osaki, Y., & Meyer, F. 2003, A&A, 401, 325
Pandel, D., Córdova, F. A., Mason, K. O., et al. 2005, ApJ, 626, 396
Patterson, J. 1999, in Disk Instabilities in Close Binary Systems. 25 Years of the Disk-Instability Model. Proc. of the Disk-Instability Workshop, ed. S. Mineshige & J. C. Wheeler (Universal Academy Press, Inc.), 61
Pilarčík, L., Wolf, M., Zasche, P., et al. 2018, NewA, 60, 1
Pratt, G. W., Hassall, B. J. M., Naylor, T., et al. 1999, MNRAS, 309, 847
Press, W. H., Teukolsky, S. A., Vetterling, W. T., et al. 1992, Numerical Recipes in FORTRAN. The Art of Scientific Computing (2nd ed.; Cambridge Univ. Press)
Qian, S. B., Han, Z. T., Fernández Lajús, E., et al. 2015, ApJS, 221, 17
Ramsay, G., Córdova, F., Cottam, J., et al. 2001a, A&A, 365, L294
Ramsay, G., Poole, T., Mason, K., et al. 2001b, A&A, 365, L288
Ramsay, G., Wood, M. A., Cannizzo, J. K., et al. 2017, MNRAS, 469, 950
Ricker, G. R., Vanderspek, R., Winn, J., et al. 2016, SPIE, 9904, 99042B
Ricker, G. R., Winn, J. N., Vanderspek, R., et al. 2014, SPIE, 9143, 914320
Ricker, G. R., Winn, J. N., Vanderspek, R., et al. 2015, JATIS, 1, 014003
Robinson, E. L., Shetrone, M. D., & Africano, J. L. 1991, AJ, 102, 1176
Scaringi, S., Groot, P. J., & Still, M. 2013, MNRAS, 435, L68
Schaefer, B. E. 2024, ApJ, 966, 155
Schoembs, R. 1986, A&A, 158, 233
Smak, J. 2013, AcA, 63, 369
Tody, D. 1986, SPIE, 627, 733
Tody, D. 1993, ASPC, 52, 173
Vogt, N. 1974, A&A, 36, 369
Vogt, N. 1982, ApJ, 252, 653
Vogt, N., Schoembs, R., Krzeminski, W., et al. 1981, A&A, 94, L29
Völschow, M., Schleicher, D. R. G., Banerjee, R., et al. 2018, A&A, 620, A42
Völschow, M., Schleicher, D. R. G., Perdelwitz, V., et al. 2016, A&A, 587, A34
Warner, B. 2003, Cataclysmic Variable Stars (Cambridge Univ. Press)
Whitehurst, R. 1988, MNRAS, 232, 35
Whitehurst, R., & King, A. 1991, MNRAS, 249, 25
Wood, J. H. 1990, MNRAS, 243, 219
Wood, J. H., Horne, K., Berriman, G., et al. 1989, ApJ, 341, 974
Wood, J. H., Irwin, M. J., & Pringle, J. E. 1985, MNRAS, 214, 475
Wood, M. A., Still, M. D., Howell, S. B., et al. 2011, ApJ, 741, 105
Wood, M. A., Thomas, D. M., & Simpson, J. C. 2009, MNRAS, 398, 2110
Woudt, P. A., & Warner, B. 2009, MNRAS, 400, 835